Modeling, Identification, and Control of Micro-Sensor Prototypes

Robert M'Closkey*
Associate Professor
Mech. & Aero. Engineering
University of California, LA
rtm@obsidian.seas.ucla.edu

A. Dorian Challoner
Scientist
Boeing Satellite Systems
El Segundo, CA
anthony.d.challoner@boeing.com

Abstract— **Micoelectromechanical systems (MEMS) are stimulating the move of modern digital control "on-chip" for a growing number of sophisticated applications. One such application is microinertial sensors of ever increasing capability bringing inertial awareness to virtually anything that moves. Modeling, identification and control of this particular genre of MEMS developed through a Boeing and UCLA collaboration is presented as an illustration on the rising edge of this revolutionary transition in the realization and theory of modern control systems.**

I. Introduction

The growing sophistication of microelectromechanical systems (MEMS) is creating new opportunities for the development and application of modern digital control systems. In an interesting application area to be discussed, sequentially produced precision mechanical plants, with expensive 3D, point-by-point material removal are being replaced with massively parallel, wafer-level, 2-D micro-machined silicon plants with integrally-machined sensors and actuators and integral low power digital control. Chips with increasingly sophisticated designs will replace their much larger, conventional 3D counterparts, and with astonishing performance. The convergence of a precision mechanical plant along with sensors, actuators and the capability for highly complex and effective control computation on a single chip will revolutionize control system engineering as digital wireless chips have already done in communication engineering. For a growing number of sophisticated control systems applications nothing will be "off-chip." With such a revolution in control system realization can theory remain invariant?

The MEMS application area discussed in this paper is inertial sensing leading to autonomous navigation for virtually anything that moves, analogous to wireless communication applications driving digital System on Chip or SOC. The plant in this case is a precision inertial proof mass. Every element and phase of modern digital controls: plant, sensors, actuators, and computation, including plant model identification, self-test and adaptation will be distilled into a photo mask set. This transformation of modern digital control will converge advanced silicon micro machining as it evolves from simple analog servos with sophisticated on-chip low-power digital signal processing driven by wireless communications. These new digital control system realizations with

every element in the loop in trade, including mechanical plant, will give rise to new control paradigms and theories to maximize performance per square mm of silicon real estate – the new control system performance index.

One application area of MEMS inertial sensors as performance improves will be for satellite attitude control. Since the beginning of the space age, zero-g attitude stability has been a major concern leading the early Syncom satellite designers, in the absence of on-board digital computers, to spin stabilize the entire satellite. It was so well balanced against radiation pressure that remarkable drift rates < 0.001 deg/h were achieved in the early 60's. This quality of passive stability enabled ground based readout of attitude sensor telemetry and spin-synchronous thruster pulse precession for adjustment of attitude during orbit injection and on-orbit from time to time for attitude maintenance. The emerging satellite communications era soon placed demands for narrow, high power earth pointed beams and hence greater control system sophistication. However, it was not until the late 80's that simple analog servos finally gave way to on-board three-axis digital control implemented in central microprocessors linking a number of attitude sensors and actuators. As the availability of capable digital hardware increases and the performance demands increase the transition to modern digital control is natural for optimized performance, improved robustness, increased versatility and design re-use, etc. This transition pertains increasingly to all system levels and can soon be anticipated for demanding MEMS applications, including inertial navigation as basic sensor performance improvement warrants. Even complete single-chip satellites have been contemplated by JPL and The Aerospace Corporation [7]. Might initial realizations also be spin-stabilized like Syncom?

Modern digital control theory and practice was born in the 60's from a potent mixture of applied mathematics and the new ability to do centralized digital computations in real time and the ever present need to improve the performance of high value plants ($10M to $100M's) in manufacturing, military and aerospace domains. The lathe and milling machine were then the enabling factors of production for the precise mechanical plant, sensor and actuator units warranted by modern digital control. Serial production of the required equipment with near "atom-at-a-time" material removal was not a limitation for such high value systems. Sensing and actuator units were distributed about the usually massive

plant and interconnected with the central processor (e.g. IBM 7090 or 360) with wire harnesses. The exorbitant expense of custom control system development would begin with a system block diagram and end in the source code for the centralized processor being the prized domain of the control system engineer. Increasingly, with the advent of semiconductor technology the cost of signal processing within the sensors and actuators and the speed and size of central processors improved by orders of magnitude enabling modern control systems to be embedded in more and smaller plants. Still the high cost of a custom digital control system development in the last century seemed an invariant, e.g. $5M for the three-axis attitude control of the Communications Technology Satellite, perhaps a $60M plant c. 1976. Curiously, because of absence of space qualified computers a 500-IC digital differential analyzer paradigm was used for control system realization (this counterpoint between the centralized algorithms of digital control implemented on "mainframes" and the distributed algorithms found in constrained realizations continues in the on-chip era). The high cost of these conventional control systems was largely because of the significant engineering teams needed for custom selection, procurement and integration of the several discrete sensor and actuator units into the physical plant as well as the centralized coding developed initially with sophisticated analytic models of the plant and finally on some sort of end-to-end or closed loop system test-bed for validation. These plant models would begin with conceptual models of the sensor, actuator and plant dynamics derived from physical principles or extensive system identification involving some version of the open loop plant. For aerospace vehicles this was not possible so sophisticated real-time digital mixed simulation systems evolved with sophisticated dynamics models to develop and then validate the final central control code.

For today's terrestrial platforms or plants such as computer disk drives or automobile engines the shear production volume can now warrant the expense of modern digital control system development and integration for $100-1000 consumer products. MEMS are now opening up the possibility of simple control systems on a chip, e.g. accelerometers or gyroscopes, in the $1-10 range and some are already on the market for safety systems and stabilization applications using simple analog servos for proof mass control. The ADXL accelerometer and ADXRS gyroscope from Analog Devices, in Figs. 1 and 2, respectively, perhaps best illustrate the state of the art of on-chip control in MEMS. Most of the sensor processing is open loop and only the gyroscope has analog closed loop control on-chip to regulate the drive amplitude. The polysilicon BiMOS fabrication process, with thin films for the mechanical proof mass grown in-situ along with the electronics, is adequate for the application intended. Bulk micro-machined gyroscopes, with proof masses etched from standard crystal silicon wafers and separately fabricated

electronics, such as the Draper tuning fork gyro [8] in Fig. 3, and Boeing/JPL post/cloverleaf gyro, shown in Figs. 4 and 7 and discussed in the sequel, have demonstrated one to two orders of magnitude better drift performance enabling tactical navigation performance with GPS aiding. The tuning fork drive is closed loop but output axis is open loop while the mechanically tuned post/cloverleaf has both drive and output loops closed, originally with discrete analog electronics. Both loops have now been realized in an off-chip low-power digital CMOS ASIC [5], [6], [3]. The notable BAE silicon ring gyroscope [4] is also a mechanically tuned design with closed-loop drive and output control. It employs a crystal silicon bulk-micromachined structure and was initially electromagnetically sensed and controlled. The latest generation is electrostatically forced and both the sensor excitation and output remain closed-loop. The Systron-Donner quartz rate sensor, Fig. 5, is a double tuning fork design quite similar in principle to the Draper single tuning fork. The current generation has an ~ 11 mm long fork and is etched from quartz wafers and employs piezoelectric sensing and control [16]. The in-plane drive tines are controlled similar to a crystal oscillator with an automatic gain control loop (not shown) while the pickup tines sense the out-of-plane Coriolis force arising from in-plane inertial rate along an axis normal to the velocity of the tip masses of the driven tines. One suitable entry for modern digital control on chip is thus to add value to the increasingly more precise and sophisticated MEMS emerging for autonomous navigation in the 3D world. This paper then reviews the modeling, identification and control performed at UCLA for the Boeing/JPL MEMS gyros from the viewpoint of this emerging transition to higher performance designs and modern digital control systems on a chip.

II. VIBRATORY RATE SENSORS

A. *Theory of operation*

A generic linear model for vibratory rate sensors consists of a two degree-of-freedom (DOF) system with a skew-symmetric matrix that is modulated by the angular rate of rotation of the sensor:

$$M\ddot{\vec{x}} + D\dot{\vec{x}} + \Omega S\dot{\vec{x}} + K\vec{x} = \vec{f}. \tag{1}$$

In this model M, D, and K are the real, positive definite 2×2 mass, damping, and stiffness matrices, respectively, and Ω and $\vec{f} = [f_1, f_2]^T$ represent the sensor angular rate of rotation and applied actuation forces, respectively. These equations are written in the sensor-fixed coordinates denoted by $\vec{x} = [x_1, x_2]^T$ and the forces $\vec{f}$ are co-located with the sensing pickoffs. The reader is referred to [11] for a detailed introduction to vibratory rate sensors. A more complete description of the sensor dynamics would include nonlinearities. A common nonlinearity in these sensors arises from elastic stiffening for sufficiently large harmonic forcing in a neighborhood of the modes. Other nonlinear contributions can depend on the
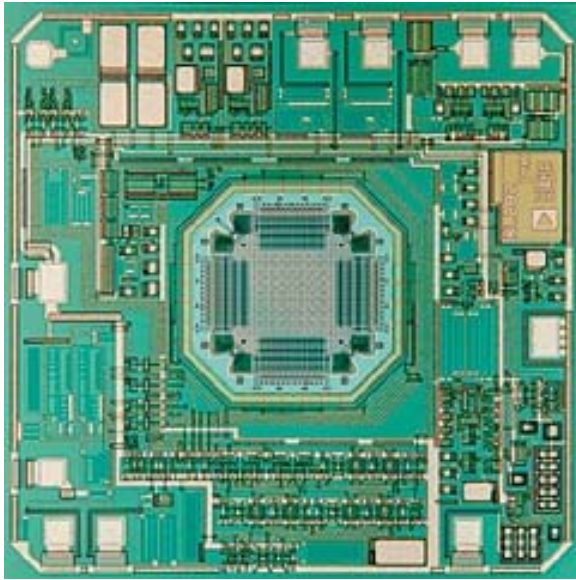
Fig. 1. In the Analog Devices ADXL accelerometer, the electronics occupy the majority of the 3 mm^2 chip area. The 2-axis device is not only extremely small, but also modest in power requirements and can measure both static and dynamic acceleration. Operation is open loop.
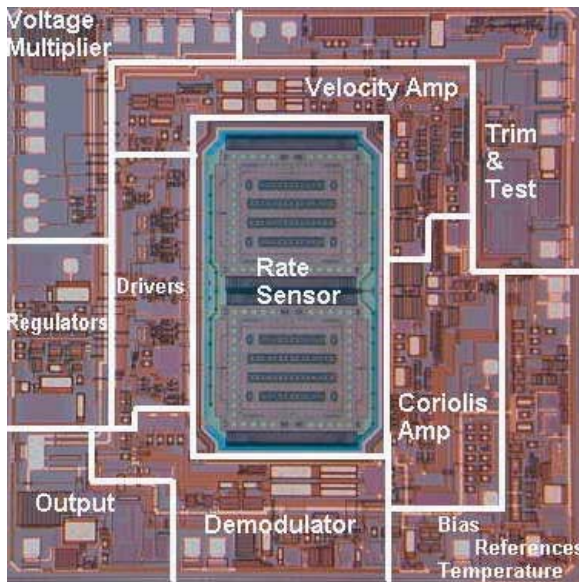

Fig. 2. The iMEMS ADXRS angular rate-sensing gyro from Analog Devices integrates an angular rate sensor and signal processing electronics onto a single piece of surface-micromachined silicon. Drive axis velocity control for the Coriolis sensor is implemented on-chip but the output axis, however, is open loop. Some on-board trim and test and perhaps bias thermal compensation are also noted.
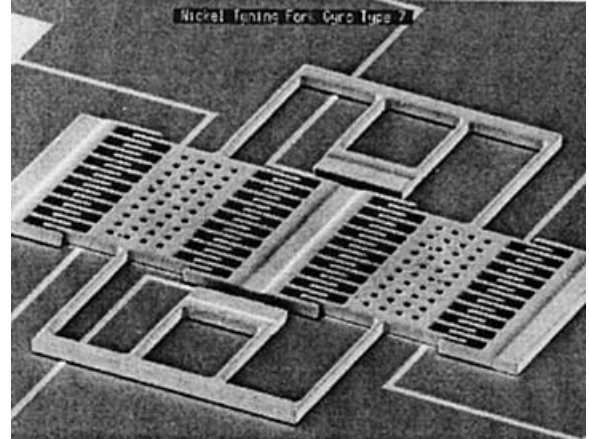

Fig. 3. The Draper tuning fork gyroscope micromachined from bulk or crystal silicon uses off-chip electronics for closed loop control of in-plane drive amplitude of the two electrostatic comb-driven proof masses. Output axis operation is open loop and comprises capacitive sensing of out-of-plane proof mass motion due to Coriolis force arising from in-plane inertial rate along an axis normal to the drive axis.
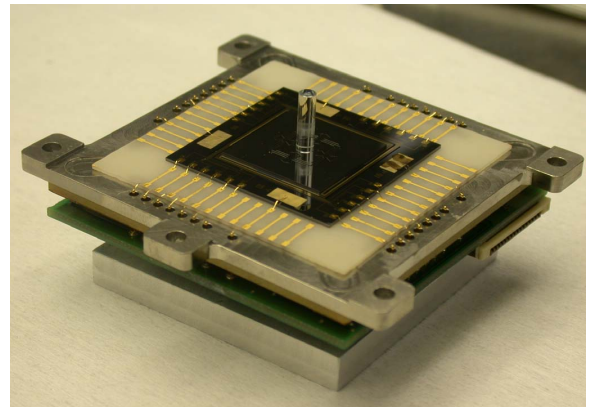

Fig. 4. Boeing/JPL Post Resonator Gyroscope (PRG) is a mechanically tuned design employing closed loop control on both the drive axis to regulate amplitude and on the output axis to sense inertial rate. The post proof-mass is rocked about one of the in-plane axes, the drive axis, using electrostatic sense and actuation and the Coriolis force arising from an out of plane inertial rate is electrostatically sensed and rebalanced about the second in-plane axis, or output axis.

manner in which forces are applied: electrostatic forces, for example, produce a softening spring effect. Linear models, however, are quite adequate for describing the dynamics of the Boeing/JPL sensor so we will not consider any further the nonlinear elements associated with the sensor's dynamics.

Control forces excite x_1 into a sinusoidal response –this is usually accomplished by a *drive* control loop– then rotation at angular rate Ω about the sense axis transfers momentum from one DOF into the other DOF resulting in a change in amplitude and phase of x_2 from which Ω may be inferred. In practice, a second control loop is used to null the x_2 pickoff signal and in this case the control effort is related to Ω. The
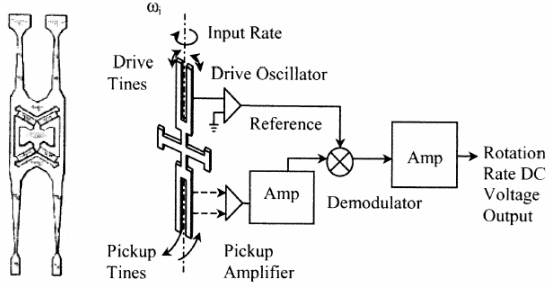
Fig. 5. Systron-Donner quartz rate sensor (QRS) is a double-tuning fork etched from quartz with piezoelectric sensing and control. Current generation ~ 11 mm long fork is depicted on the left. Closed-loop automatic gain control maintains oscillation of the drive tines while the output axis comprises open-loop sensing of motion of the pickup times.

Fig. 6. Angular rotation rate is depicted as a feedback loop around the mechanical dynamics of the gyro.

second loop has been termed the *force-to-rebalance* loop or simply, rebalance loop, in the literature. These two control loops are common in vibratory rate sensors although their implementation may differ from one technology to another.

Analysis of the closed-loop signals illuminates certain limitations imposed on the detection of Ω so consider the closed-loop system in Fig. 6. All signals have dimension two in this diagram, and for steady state analysis we take Ω to be constant. Furthermore, we assume a sinusoidal steady-state is achieved after injection of an appropriate reference r so it is convenient to represent the sensor model with its frequency response function for this analysis,

$$\tilde{P} = (I - j\omega PS\Omega)^{-1} P,$$

where

$$P = \left(-\omega^2 M + j\omega D + K\right)^{-1}.$$

The control force generated by feedback relative to the sensor output is $\vec{f} = \tilde{P}^{-1}\vec{x} = P^{-1} + j\omega S\Omega$. In order to detect Ω, the second component of the control force, denoted f_2, is observed. This is merely the $(2,1)$ component of $\tilde{P}^{-1}\vec{x}$ which is obtained from the figure or the original equations (1),

$$f_2 = (-\omega^2 M_{21} + j\omega D_{21} + K_{21} + j\omega S_{21}\Omega)x_1 +$$
$$(-\omega^2 M_{22} + j\omega D_{22} + K_{22})x_2.$$

The matrix subscripts denote the component of interest. In an ideal sensor the off-diagonal terms in the mass, stiffness and damping matrices are zero and if we further assume that the controller gain is sufficiently large at ω rendering $x_2 \approx 0$ then as a first order approximation the feedback force is proportional to Ω and may be obtained by demodulating f_2 with respect to $\dot{x}_1$. In a non-ideal sensor, the off-diagonal damping produces a component in f_2 that is in-phase with the Ω-induced component. This represents a spurious rate that cannot be distinguished from the actual rate and this is the primary reason that damping is minimized to the greatest degree possible in high performance vibratory rate sensors. The off-diagonal mass and stiffness matrix produce
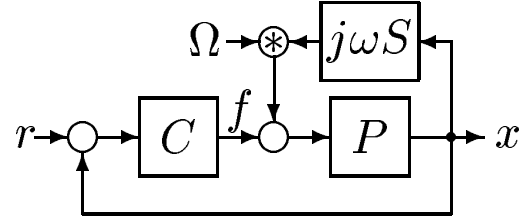
terms which are $90°$ out of phase (quadrature) with the Ω-induced terms and hence may be rejected by phase-sensitive demodulation with respect to $\dot{x}_1$. In a loop with finite gain at ω, however, the quadrature and in-phase errors are further exacerbated by the fact that $x_2 \neq 0$. The non-idealities in the sensor dynamics that produce rate-sensing errors are itemized in [18], [19] for some simple models and can be identified according to their influence on the system matrices.

This analysis shows that even with feedback, the error in the rate estimate can be sensitive to plant perturbations so it is fair to question the of role feedback in this application. One should understand that the art of inertial instrument design resides in the ability to make plant perturbations zero, or at least fixed, as a function of time, temperature, vibration in the operating environment, etc. Feedback, however, is useful for a number of reasons even though it does not mitigate plant uncertainty for this particular problem. Here are a few points justifying its use:

1) Feedback assists in generating an approximate plant inverse for the detection of Ω. The complexity of the feedback filters is often less than the complexity of a "deconvolution" filter that would be required in an open-loop setting.
2) It is sometimes possible to replace "mechanical" stiffness with "servo" stiffness with the benefit of the servo stiffness being less susceptible to temperature effects and possessing less hysteresis.
3) A high gain rebalance loop keeps the x_2 signal near zero, thereby improving the linearity of the response and simplifying calibration algorithms.
4) In a high gain loop where $x_2 \approx 0$, the quadrature terms in f_2 are $(-\omega^2 M_{21} + K_{21})x_1$ and hence may be determined by demodulating f_2 with respect to x_1. This is essentially provides an on-line identification scheme of the quadrature terms.

The last point deserves more elaboration. The quadrature component can be eliminated by orienting the generalized eigenvector of M and K associated with the driven mode such that it's projection onto the x_2 pick-off is zero, and also by reducing the frequency split between the modes.

Both methods are pursued in practice by a variety of tuning schemes that perturb the mass and stiffness matrices. A complementary method is to change the sensing pickoff frame by creating weighted sums of the pickoff signals. This approach leaves the plant dynamics unchanged but modifies the sensor and actuator location on the vibrating structure. Whatever method is employed, it is often necessary to keep the quadrature signal small to avoid saturation of the rebalance loop amplifiers and to mitigate the effect of demodulation phase error, and so most high performance sensors employ a *quad-nulling* loop.

B. Boeing/JPL micromachined gyro overview

The foregoing discussion is general and applies to any vibratory gyroscope. We discuss in this survey, however, many interesting system identification and control issues for a particular class of sensors: the Boeing/JPL micromachined gyroscopes. This section provides some details on the physical aspects of these sensors. The Boeing/JPL microgyros (Fig. 7) consist of a silicon micromachined plate suspended above a set of electrodes. The two modes that are exploited in angular rate detection correspond to a two degree-of-freedom rocking motion of the plate that is parameterized by the θ_1 and θ_2 angular coordinates in Fig 7. The central post strongly couples these rocking degrees of freedom via a Coriolis term (the axis which is sensitive to angular rates is the Ω-axis along the post). Various electrodes are used to apply electrostatic forces at points on the plate or, as the plate deflects relative to the electrodes, capacitive sensing is used to measure the deflection. More details on the design and fabrication of these sensor may be found in [1], [21], [22], [23].

Relatively weak electrostatic forces are used to excite the sensor dynamics so an appreciable response amplitude can only be achieved when the excitation power is concentrated in a neighborhood of the lightly damped sensor modes. Thus, it is necessary that the drive loop selectively excite one of these modes, preferably at the frequency of maximum response because this make use of the sensors intrinsic gain. As mentioned in Section II-A there are advantages in designing the sensor so that $\omega_1 \approx \omega_2$. The Boeing/JPL fabrication process aims to produce sensors with these degenerate dynamics and in fact can consistently produce devices with frequency splits on the order of 0.2%.

There are multiple electrodes on the baseplate that can be configured as sense pickoff or actuators. Two of these electrodes are selected for sensing, another two electrodes are designated as actuators, and the remaining electrodes are used for applying bias voltages to further reduce the detuning between the modes. The actuation electrodes, also commonly referred to as the *drive* electrodes, can be driven directly from a function generator or digital-to-analog converter (DAC). The sensing electrodes use a trans-impedance op-amp configuration to provide a buffered output voltage that

is proportional to the velocity averaged over the distributed electrode. Maximum displacements of the sensor's elastic structure, on the order of 1 to 2 μm, correspond to sense electrode potentials of several hundred millivolts in the frequency range of the important modes discussed below. When defining the equations of motion of this structure we focus on the two closely spaced rocking modes that can be modeled by (1) although we do not use angular coordinate parameterization in Fig. 7. Instead, the following perspective is adopted: the generalized coordinates are chosen to be the coordinates established by the sensing electrodes; if we denote the sensing electrode measurements as S_1 and S_2 then $[\dot{x}_1 \quad \dot{x}_2] := [S_1 \quad S_2]$; the electrostatic forces created by the potentials applied to the pair of drive electrodes, denoted D_1 and D_2, are different from the generalized forces $[f_1, f_2]$ of (1) since the drive electrodes and the sensing electrodes are not colocated. Thus, we modify (1) to

$$M\ddot{\vec{S}} + C\dot{\vec{S}} + K \int \vec{S} = B\vec{D}, \qquad (2)$$

where $\vec{S} := [S_1, \quad S_2]^T$, $\vec{D} := [D_1, \quad D_2]^T$, and B is a real, non-singular 2×2 matrix that specifies how the force applied by each drive electrode couples into the coordinate frame specified by the sensing electrodes. The Coriolis term has been omitted from this equation.

III. THE MICRO-SENSOR RESEARCH PARTNERSHIP BETWEEN UCLA, BOEING AND JPL

As discussed in the Introduction, there has been an ever-present demand for high quality inertial stabilization for long-life satellite applications involving narrow-beam payloads. Gyroscopes, of the spinning mass variety, were initially qualified for intermittent operation during thrusting maneuvers. In the early 1990's Delco Systems, a division of then Hughes Aircraft Company completed the development and qualification of the first continuous duty solid state gyroscope for satellites, the quartz Hemispherical Resonator Gyroscope (HRG). This was a conventionally-machined, precision tuned Coriolis vibratory sensor with capacitive sensing and actuation and closed loop drive and output axis control. Northrop-Grumman now owns and manufactures the HRG.

As the HRG was being developed and qualified for space applications, Kaiser and Tang [21] at JPL were experimenting with novel bulk silicon micromachined inertial sensors based on tunneling and capacitive sensing techniques. Kubena at then Hughes Research Laboratories, experimented with methods of fabricating tunneling sensors using surface micro-machined nickel beams on a silicon substrate. This led to tunneling rate sensor and accelerometer designs with closed loop output control being developed for the then Hughes Space and Communications unit, now Boeing Satellite Systems (BSS), see [9], [10]. With the advantages of conventional vibratory gyroscopes for space established by the HRG, the promise of MEMS was then to significantly reduce cost,
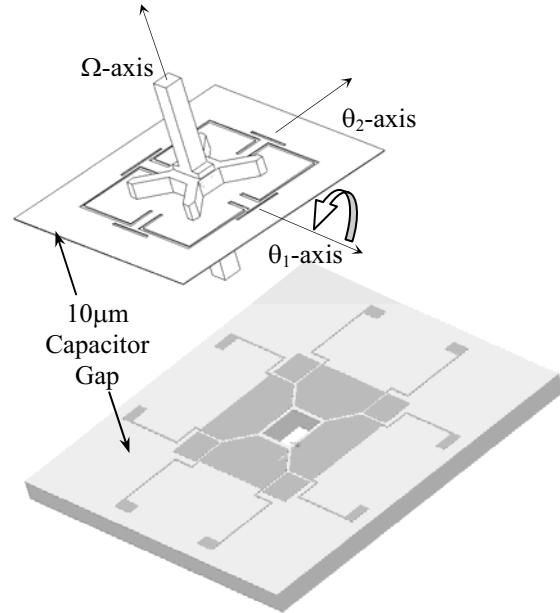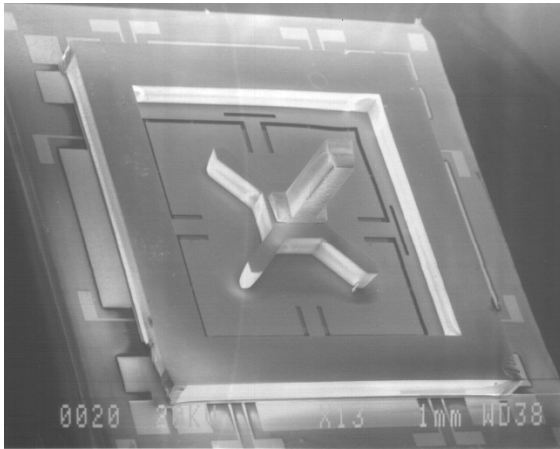
Fig. 7. A photo of the Boeing/JPL vibratory gyro prototype (left) and drawing indicating baseplate electrode layout (right). The cloverleaf structure is clearly visible in the photo and has three prominent modes that can be parameterized as two angular deflections θ_1 and θ_2, and an out-of-plane linear translation in the direction of the Ω-axis. The post along the Ω-axis strongly couples the two angular degrees of freedom with a Coriolis term and it is this coupling that is exploited for detection of the sensor's angular velocity resolved along the Ω-axis. The shaded area on the baseplate drawing reveals the electrode layout.
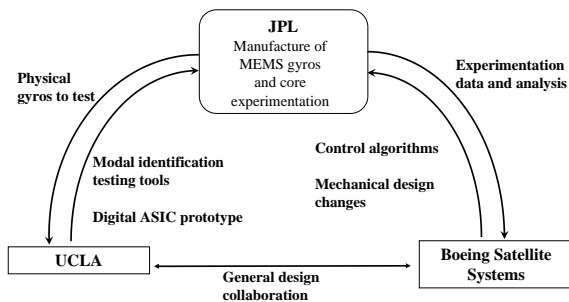

Fig. 8. Boeing MEMS technical cooperation and partnership with JPL and UCLA.

weight and power. By 1997, BSS had begun a partnership with JPL on the development of advanced silicon MEMS gyroscopes for space and with UCLA on complementary modeling, identification and control of MEMS. The triad shown in Fig. 8 sketches out the contribution of each group. UCLA work under UC MICRO grant funding from BSS, the National Science Foundation and the Jet Propulsion Lab, is discussed in the remainder of this paper.

A. *Micro-sensor system identification*

System identification plays an important role in not only providing feedback compensation design models but also gives critical information during post-manufacturing steps during which the detuned natural frequencies of the sensor

modes can be reduced by application of bias voltages to special electrodes on the baseplate. The bias voltages actually perturb the sensor dynamics by creating a force field that produces an equivalent negative spring rate. Proper adjustment of the bias voltages pulls the rocking mode frequencies closer together.

A typical wide-band experimental frequency response is shown in Fig. 9. The sensor is tested as a 2-input/2-output system and in this case $\Omega = 0$. The sensor/actuator pairs are indicated in the title of each subplot. The resonance that corresponds to a linear translation of the sensor's elastic structure along the post direction occurs near 2700 Hz. This mode is not only easily excited by the control electrodes, but also by linear acceleration in the appropriate direction. The next lightly damped resonance near 4420 Hz actually comprises the two "rocking" modes of the cloverleaf. The frequency split between these modes is less than 5 Hz (0.11%) and so each mode cannot be individually resolved on this scale. It is these modes that are strongly coupled via the Coriolis acceleration when the sensor is rotated. Although the sensor was designed to exploit these two modes for angular rate sensing, it is quite evident that the wide-band sensor dynamics are far richer than (2). Nevertheless (2) is an appropriate description if one is interested in a narrow frequency window around the modes. The remaining lightly damped resonances above 5 kHz are other flexural modes in the sensor's elastic structure. Parasitic capacitance between
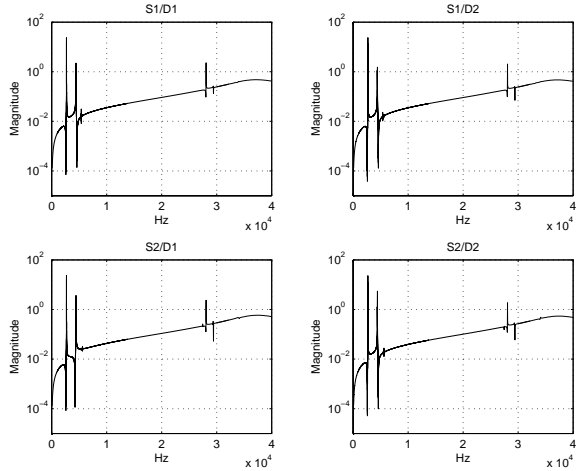
Fig. 9. Wide-band frequency response of the rate sensor. The modes that are exploited for detection of Ω are clustered near 4.4kHz. There is another significant mode near 2.7 kHz that also requires active control.
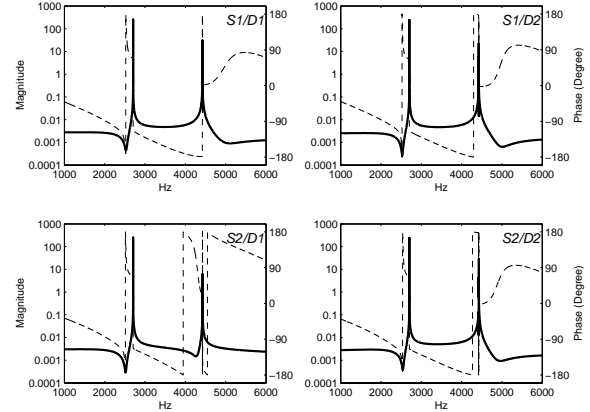

Fig. 10. Frequency response of an ARX model identified from 5 seconds of I/O data (solid: magnitude; dash: phase). The sensor dynamics are excited with periodic, independent chirp sequences with power focused in the 2.5 kHz to 5 kHz band. This span includes the modes of interest and leads to a high-quality model that can be further analyzed. There is a single mode near 2.7 kHz that corresponds to cloverleaf structure vibrating in a direction corresponding to the Ω-axis in Figure 7. The two rocking modes are clustered near 4.4 kHz.

the drive electrodes and sense electrodes causes the positive trend in the slope up to 35 kHz at which point the signal conditioning amplifiers roll-off. Lastly, the sharp notches in close proximity to the modes near 2700 Hz and 4420 Hz are created by a charge cancellation on the sensing electrodes due to the opposite phase of parasitic capacitance-induced charge and the charge created by motion of the cloverleaf. These plots were produced by concatenating results from multiple tests with a dynamic signal analyzer and require a significant time investment.

Although Fig. 9 represents the generic features for this class of rate sensor, it is not necessary to test the devices over such a large frequency range since it is the Coriolis-coupled modes that must be quantified. Furthermore, even though all of the channels in Fig. 9 look similar, there do exist significant differences in the frequency responses in a neighborhood of the two rocking modes. This region must be examined more closely. Our solution to use an adaptive lattice filter for fitting a high-order two-input/two-output ARX model was motivated by the fact that accurate, rapid estimates of the two rocking modes be available for post-fabrication tuning. The object was to supplant the arduous and time consuming single-channel testing that was done with a commercial signal analyzer. The main objection to using the signal analyzer was the excessive testing times required to produce results of adequate frequency resolution. The test data sets for the ARX modeling are generated by exciting the drive electrodes with periodic, but independent, chirp sequences. The chirp power is concentrated from 2 kHz to 5 kHz in order to excite the translational mode near 3 kHz in addition to the rocking modes at 4.4 kHz. The buffered sense electrode signals are synchronously sampled at 50 kHz. Relatively high ARX model orders (≈ 40) are

necessary for capturing not only the "rigid body" dynamics of the cloverleaf but also the dynamics of the pre-amps, anti-aliasing filters (8-poles/channel, two channels) and other sensor modes outside of the input power band that are nevertheless excited by vibration of the sensor case. The high model orders ensure that the modes we want to identify are estimated with little bias. Some of this work is reported in [15]. Another fact that should not be overlooked is the *multichannel* nature of the experiments and models: as the frequency split between the two rocking modes is reduced, the single channel identification problem becomes very ill-conditioned due to the fact that in the degenerate case, the sensor dynamics are unobservable and uncontrollable from any SISO pairing of sensors and actuators. A frequency response of the ARX model is shown in Fig. 10. The translational mode and two rocking modes are captured. Figure 11 shows the frequency response detail in a neighborhood of the rocking modes. The phase includes lags from the anti-alias filters.

As an application of the ARX modeling consider Fig. 12. These pictures represent measurements of the vibrating cloverleaf measured by optical interferometry. The sensor is excited at each of its modal frequencies and then the steady-state response of the cloverleaf surface is strobed at different phases relative to the sinusoidal excitation –this builds map of the surface displacement throughout its periodic response. The green bands indicate regions of zero displacement, so in fact the cloverleaf is "rocking" about these axes. These essentially reveal the generalized eigenvectors of the mass and stiffness matrices since the transient time constants are larger than the frequency split. This can be argued as follows. Consider (2) and let T be the matrix whose columns are
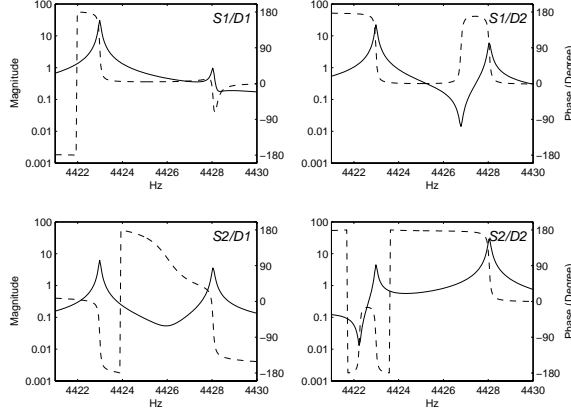
Fig. 11. Zoomed version of Figure 10 showing the frequency response detail in in a neighborhood of the rocking modes. The model includes the anti-aliasing filter lag so the phase is not asymptotic to $\pm 90°$ as would be expected from (2).

the generalized eigenvectors of M and K, i.e. $MT\Lambda = KT$ where $\Lambda = \text{diag}(\omega_1^2, \omega_2^2)$ are the eigenvalues arranged on the diagonal. Furthermore, $T^T MT$ and $T^T KT$ are both diagonal with diagonal elements (m_1, m_2) and (k_1, k_2), respectively, and $\omega_p^2 = k_p/m_p$, $p = 1, 2$. The transformed damping matrix $T^T CT$, however, is not diagonal in general and so it is represented by

$$T^T CT = \begin{bmatrix} c_1 & c_3 \\ c_3 & c_2 \end{bmatrix}.$$

The frequency response of (2) then becomes

$$\begin{bmatrix} -m_1\omega^2 + k_1 + jc_1\omega & jc_3\omega \\ jc_3\omega & -m_2\omega^2 + k_2 + jc_2\omega \end{bmatrix} T^{-1}\hat{S} = j\omega T^T B\hat{D},$$

(3)

where $\hat{}$ denotes the frequency response representation. When $\omega = \omega_1$ (3) simplifies to

$$\hat{S} = T \begin{bmatrix} c_1 & c_3 \\ c_3 & jm_2\Delta_\omega + c_2 \end{bmatrix}^{-1} T^T B\hat{D},$$

$$= \frac{1}{\delta} T \begin{bmatrix} jm_2\Delta_\omega + c_2 & -c_3 \\ -c_3 & c_1 \end{bmatrix} T^T B\hat{D},$$

where $\Delta_\omega := (\omega_2^2 - \omega_1^2)/\omega_1 \approx \omega_2 - \omega_1$ and $\delta = c_1 c_3 - c_2^2 + jc_2 m_2 \Delta_\omega$. The last expression is informative because it demonstrates that the steady state response of sensor is essentially a scaled version of the *first* column of T when

$$m_2 \Delta_\omega >> c_p, \quad p = 1, 2, 3 \quad (4)$$

regardless of the input direction. Thus, the cloverleaf plate rocks about an axis orthogonal to the generalized eigenvector corresponding to ω_1. A similar argument can be made for sinusoidal excitation of the sensor with frequency ω_2. Note that (4) implies that the frequency split be larger than inverse of the open-loop sensor time constant (we can estimate the open-loop sensor time constants to be $m_1/c_1 \approx m_2/c_2$). When this condition is not satisfied the frequency response

is dominated by the damping when the forcing frequency is in a neighborhood of the modes.

Now turning our attention back to Fig. 12, the top two plots represent the sensor's response with zero potential on the bias electrodes. The rocking mode frequency difference in this case is approximately 3 Hz out of a nominal frequency of 4.4 kHz. The bottom two plots represent the modal responses with a non-zero potential on one bias electrode and in this case the frequency split has been reduced to less than 1 Hz. Not only have the modal frequencies changed, but also the generalized eigenvectors of M and K as indicated by a change in orientation of the green bands. It is interesting to note that the green bands, and hence the generalized eigenvectors, look roughly orthogonal for each case. This should come as no surprise since in an ideal sensor with no fabrication irregularities, the mass and stiffness matrices are scalar-times-identity so small perturbations to M and K produce a situation in which their generalized eigenvectors are nearly orthogonal.

The ARX model yields estimates of the modal frequencies as well as the generalized eigenvectors of M and K, but using only several seconds of I/O data and several seconds for fitting and analyzing the ARX model (the same assumption applies when computing the generalized eigenvector estimates, namely the frequency split is sufficiently large compared to damping constant). Fig. 13 reveals the "tuning space" for the gyro: the bias electrode potentials (denoted BT and B2 in the figure) are swept through a selected range, and I/O data are acquired at each point; an ARX model is fit to the data set and then subsequently analyzed for the modal frequency split as well as the generalized eigenvector orientation. The blue and red vectors in the figure represent the eigenvector estimates and the length of the vectors indicates the split. In this example, the split can be reduced to less than 100 mHz, and the necessary bias potentials can be obtained from the figure.

The ARX models are adequate for tuning the rocking modes but it is difficult to obtain precise estimates of the damping from short sequences of I/O data. This information, along with a more detailed picture of the mass and stiffness matrices associated with the two rocking modes, is useful in the sensor development process where, for example, the effect of a step taken during manufacturing can be analyzed for its impact on M, K, and C. This is work in-progress but we can report on an efficient method for generating very precise frequency response test data that can be used in generating the system matrices by fitting the frequency response data to (3). The idea is to use sine wave correlation testing in a neighborhood of the rocking modes for its superior noise rejection capability. Sine wave testing of the open-loop sensor, however, requires marathon durations because of the system time constants (Q can exceed 40,000 for these sensors). Even if one could tolerate the lengthy tests, the frequency *drift* exhibited by these sensors precludes

Surface Data

Mag: 0.9 X
Mode: PSI
Date: 04/06/00
Time: 15:28:59

Surface Statistics:
Ra: 430.10 nm
Rq: 521.32 nm
Rz: 1.90 um
Rt: 2.00 um

Set-up Parameters:
Size: 368 X 236
Sampling: 18.96 um

Processed Options:
Terms Removed:
None
Filtering:
None

um
0.997
0.600
0.200
-0.200
-0.600
-1.001

Title: Difference
Note:

Surface Data

Mag: 0.9 X
Mode: PSI
Date: 04/06/00
Time: 15:20:33

Surface Statistics:
Ra: 316.82 nm
Rq: 384.12 nm
Rz: 1.42 um
Rt: 1.49 um

Set-up Parameters:
Size: 368 X 236
Sampling: 18.96 um

Processed Options:
Terms Removed:
None
Filtering:
None

nm
745.443
400.000
100.000
-200.000
-747.630

WYKO
Mag: 0.9 X
Mode: PSI
Surface Data
Date: 04/06/00
Time: 16:31:58

Surface Statistics:
Ra: 767.10 nm
Rq: 1.02 um
Rz: 4.77 um
Rt: 5.12 um

Set-up Parameters:
Size: 368 X 236
Sampling: 18.96 um

Processed Options:
Terms Removed:
None
Filtering:
None

um
2.550
1.500
0.500
-0.500
-1.500
-2.566

Title: Difference
Note:

WYKO
Mag: 0.9 X
Mode: PSI
Surface Data
Date: 04/06/00
Time: 16:34:54

Surface Statistics:
Ra: 727.09 nm
Rq: 968.55 nm
Rz: 4.51 um
Rt: 4.84 um

Set-up Parameters:
Size: 368 X 236
Sampling: 18.96 um

Processed Options:
Terms Removed:
None
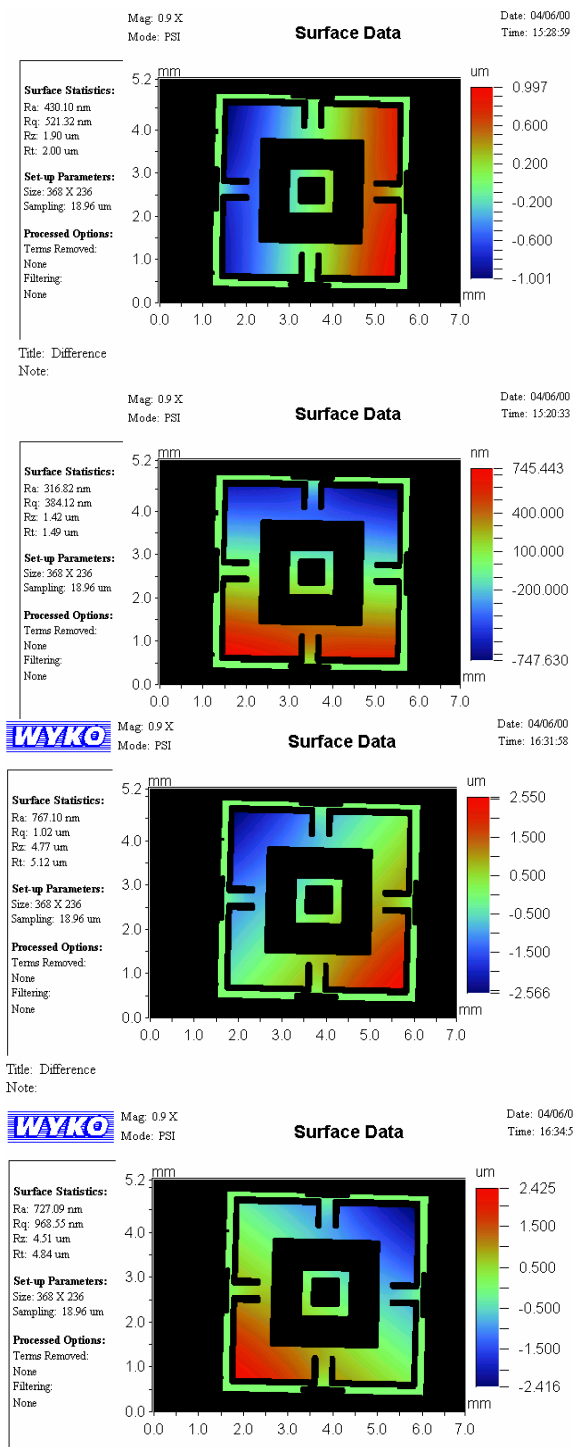Filtering:
None

um
2.425
1.500
0.500
-0.500
-1.500
-2.416

Fig. 12. Top two figures: the vibrating cloverleaf imaged with a pulsed-source interferometer when the bias potentials are zero. The green bands reveal the orientation of the generalized eigenvectors of *M* and *K*. Bottom two figures: same sensor with non-zero potentials on the bias electrodes. The modal frequencies and eigenvectors are perturbed. These experiments require optical access to the sensor and several minutes of testing.

Mode axes vs. Tuning Space (Red vect is Higher freq mode)
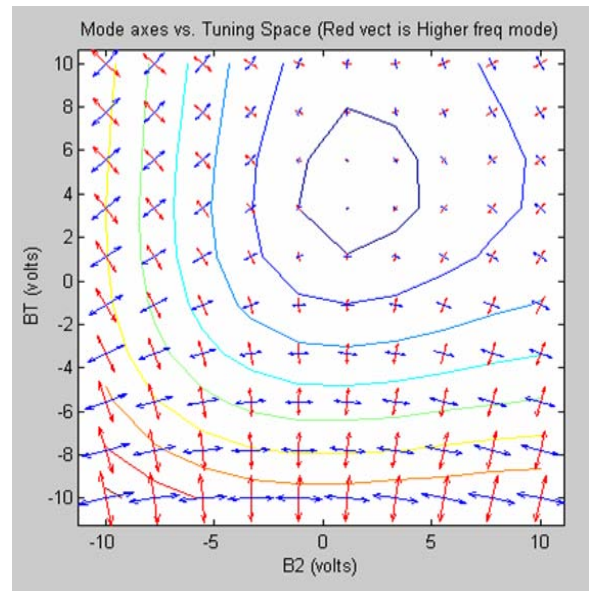
BT (volts)

B2 (volts)

Fig. 13. Tuning the modes of the sensor to degeneracy with bias electrodes.

identification experiments lasting longer than a few minutes. For example, Fig. 25 shows frequency data obtained from a tracking control loop that selectively excites one of the sensor's rocking modes to a stable amplitude independent of its frequency. A real-time readout of the operating frequency is provided by a frequency counter. This control loop will be discussed in more detail in Section III-B. One can see from the figure that an identification experiment lasting more then a few minutes risks producing worthless results because the dynamics may have substantially changed during the course of the experiment (this claim will be justified shortly).

The solution is to employ a damping controller to vastly reduce the time constants in the closed-loop to facilitate rapid identification of closed-loop frequency responses from which the open-loop sensor frequency response can be extracted. A reduced-order ARX model is used to synthesize a controller via the robust loop-shaping [17]. We won't focus on the synthesis procedure other than to note that it produces a very sensible controller from the point of view of increasing the closed-loop damping. For example, Fig. 14 is a Nyquist plot of the ARX sensor model in a neighborhood of the rocking modes (the mode near 2.7 kHz was excluded to avoid cluttering the figure –a similar argument can be made for this mode too). The two loops in each plot are the dynamics associated with the two lightly damped rocking modes and these plots reveal that both modes strongly couple into the off-diagonal channels, and to a lesser extent into the diagonal channels. The ARX model of the loop gain *PC* where *P* is the full-order ARX sensor model and *C* is the 6-state synthesized controller, is shown in Fig. 15. The intriguing features of the loop gain are that it is now diagonally dominant, each diagonal channel has a different
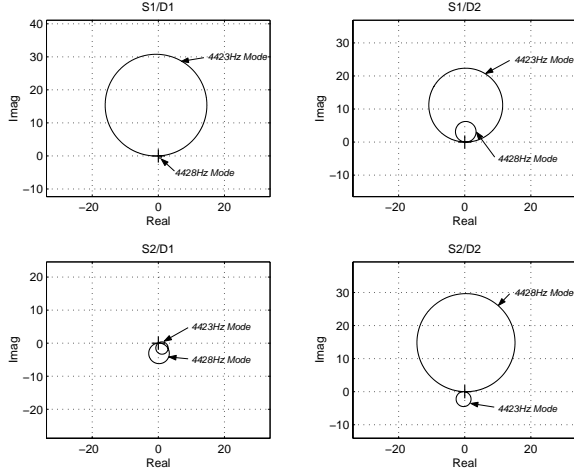
Fig. 14. Nyquist plot of the full-order ARX model from 4 kHz to 6 kHz is adapted from Figure 10. The translational mode is excluded with this frequency range.
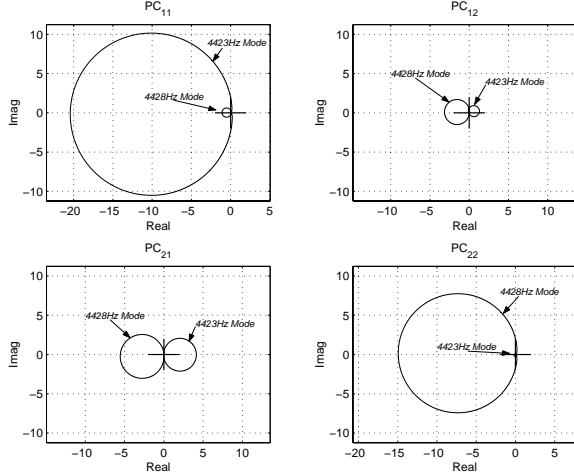

Fig. 15. A Nyquist plot of the *PC* from 4 kHz to 6 kHz demonstrates that the controller has adjusted the loop phase to emulate velocity-to-force feedback (positive feedback convention for the implementation).

dominant mode, and the phase of the dominant modes is adjusted so that the drive electrode potential is 180 degrees out of phase sense electrode measurements thereby emulating velocity-to-force feedback.

The closed-loop system time constants are reduced by over a factor of 50 compared to the open-loop sensor. Since the open-loop transients require approximately 4 seconds to ring down to 10 percent of their initial amplitude, it is necessary to wait on the order of 10 seconds to allow the transients created by switching the reference signal to decay to levels where the frequency response estimate is not affected. In contrast, the closed-loop time for transient settling is reduced to 0.2 seconds. Thus, a detailed empirical frequency response is identified in a neighborhood of the two rocking modes in
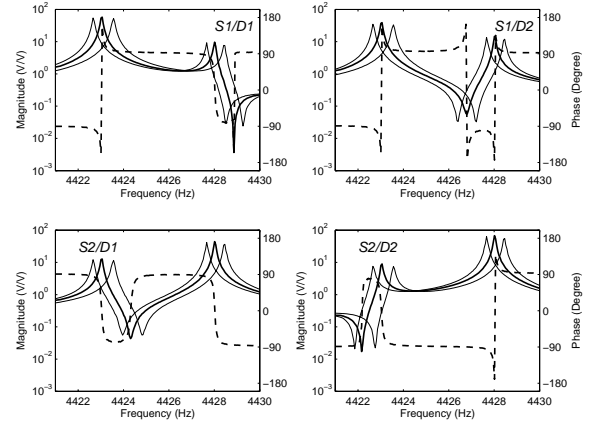

Fig. 16. The sensor's empirical frequency response in a neighborhood of the rocking modes (solid: magnitude; dash: phase). The phase plot is associated with the heavy trace. The two other magnitude plots were obtained from data sets acquired 20 minutes apart and illustrate the slowly-varying nature of the gyro dynamics.

less than 2 minutes. The closed-loop transfer functions that are identified are

$$H_1 = PC(I - PC)^{-1}, \qquad H_2 = C(I - PC)^{-1},$$

and the open-loop sensor estimate is recovered from calculating

$$P = H_1 H_2^{-1}.$$

Fig. 16 illustrates the frequency response estimates obtained from this closed-loop testing procedure. The solid and dashed heavy traces represent a "nominal" case; the two additional light solid traces represent the sensor's frequency response taken 20 minutes and 40 minutes later. Note that the dynamics slowly vary with time in such a way the frequency variable is scaled. This dependence can be observed in open-loop frequency response testing because the long durations introduce smearing of the frequency response estimate. Also note that the frequency response estimate clearly resolves the zeros –something that the ARX model has trouble capturing (compare Figure 16 to Figure 11).

This precise frequency response data can be used for further analysis. In fact, positive definite mass and stiffness matrices can be fit to the data –the damping matrix at this point is not constrained because the small parasitic capacitive coupling from the drive to sense electrodes actually biases the damping estimate. More will be reported on these efforts at a later date. The identified mass and stiffness matrices, however, do permit computation of *decoupling* transformations applied at the sensor's input and output that essentially diagonalizes its transfer matrix. Referring to (3), if a new set of outputs and inputs are defined as

$$\tilde{S} := T_{out}\hat{S}, \text{ where } T_{out} = T^{-1}$$
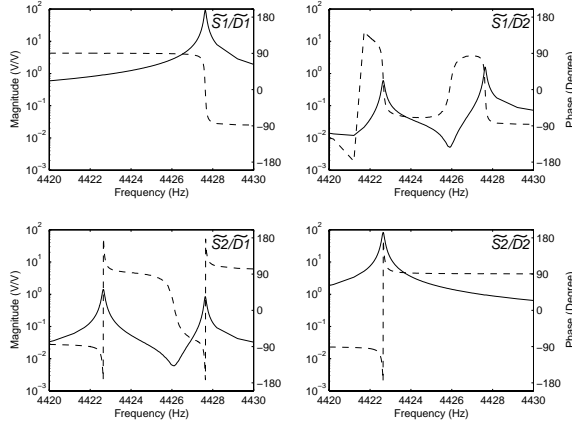$$\tilde{D} := T_{in}^{-1}\hat{D}, \text{ where } T_{in} = (T^T B)^{-1}$$

Fig. 17. Empirical frequency response of the re-identified sensor including the I/O transformations. The frequency response is now diagonally dominant with a different rocking mode in each diagonal channel.

then the transfer function $\tilde{S}/\tilde{D} = T_{out}H_{sens}T_{in}$, where H_{sens} denotes the sensor, has been diagonalized to the extent allowed by the damping matrix. Note that $\tilde{S}$ and $\tilde{D}$ are constructed from constant gain transformations of the native sense electrode and drive electrode signals. This method of diagonalizing the sensor dynamics can be used in conjunction with the tuning methods discussed earlier to reduce the quadrature signals in the closed-loop sensor. The transformations are realized with analog summing networks with programmable coefficients. The transformations are nearly orthogonal matrices (maximum condition number is 1.2) and hence do not exacerbate any modeling uncertainty associated with the frequency response data. The re-identified sensor, including I/O these transformations, is shown in Figure 17. The off-diagonal channels are now nearly 40 dB smaller (in terms of peak magnitude comparison) than the diagonal channels. This sensor is now in an ideal configuration for the design and implementation of the feedback compensation. This is the subject of the next section.

B. Micro-sensor control

Feedback compensation forms an integral part of many micro-sensors and the vibratory rate gyros are no exception. As mentioned in Section II-A, feedback does not reduce the effect of sensor uncertainties on the detection of the angular rotation rate because of the nature of the coupling of the rate into the equations of motion. Feedback, however, is useful providing an approximate inverse of the sensor dynamics and this simplifies subsequent signal processing. The primary feedback loops for vibratory gyros are:

1) *Excitation loop.* The harmonic excitation of a degree of freedom, often a lightly damped mode, to a stable amplitude is required. There are numerous methods using feedback to achieve this, including self-exciting loops and phase-locked loops. A version of a self-

exciting loop called automatic gain control is discussed in some detail below.
2) *Rebalance loop.* The "sensing" pick-off signal is nulled by a high-gain feedback loop.
3) *Quad-nulling loop.* The quadrature signal nulling loop essentially provides real-time identification of the plant dynamics, albeit at the excitation frequency only. This loop typically has low-bandwidth and compensates for perturbations of the plant dynamics that have time constants on the order of minutes or hours (thermally induced drifts, for example –see Figure 16). The actuator associated with this loop has limited authority over modifying the plant dynamics. The bias electrodes on the Boeing/JPL microgyros are used for this purpose.

The reduction in sensing element size using micromachining technology can mean reduced performance (larger rate noise density) due to relatively larger manufacturing tolerances so in order realize the advantages of MEMS sensors it is often necessary to incorporate on-chip electronics for a compact, but fully integrated and functional, sensor. Analog Devices has successfully commercialized MEMS accelerometers and vibratory angular rate sensors with complete on-chip signal conditioning, control and self-test electronics. It is understandable that the details of the algorithms, and especially their implementation, are not published by the producers of commercially available micro-sensors. The academic environment, however, has exchanged ideas on different approaches for error suppression and control. More recent efforts include [12], [20].

The Boeing/JPL post-resonator gyro (PRG) shown in Fig. 4 has demonstrated 0.1 deg/hr bias stability with discrete analog implementations of the control and signal processing components. The excitation loop in this sensor is called automatic gain control (AGC), a block diagram of which is shown in Fig. 18. The idea is simple: a measurement of the oscillator velocity is fed back to the forcer and depending of the sign of the feedback gain, the oscillation is damped (when oscillator amplitude is larger than the reference amplitude R) or destabilized (when the oscillator amplitude is smaller than the reference amplitude). The feedback gain is determined by output of the the PI compensation which is preceded by an amplitude detection scheme. When the oscillator has reached a steady-state amplitude the AGC adds the same amount of energy as is dissipated by the damping. The primary advantage to using the AGC is that it is *adaptive* due to the fact that the oscillator is always excited at ω_n, even when ω_n is slowly varying with time. The rebalance loop for the post-resonator gyro is a traditional high-gain feedback loop.

The discrete analog electronics for the PRG are effective, but not very flexible or power-efficient. Our research group at UCLA has developed, under funding from Boeing, an application specific integrated circuit (ASIC) that implements a digital AGC, rebalance loop, and signal demodulation for in-phase and quadrature component detection, in a very low-
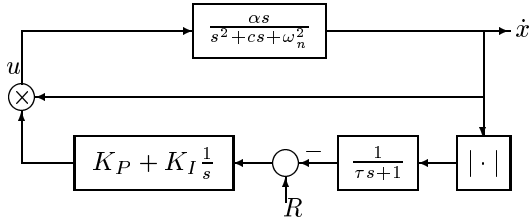
Fig. 18. Simplified AGC for self-excitation of the oscillator to a stable amplitude.

power and programmable platform. The next section provides a few details of the ASIC performance when integrated with the Boeing/JPL microgyro. Efforts to integrate the ASIC with the PRG are underway.

ASIC details

The ASIC architecture, shown in Fig. 19, employs a nonlinear automatic gain control for the drive loop, a linear filter for the rebalance loop and also provides filtering and demodulation of the rebalance signal for detection of its in-phase and quadrature components. The linear filters are realized with an FIR implementation. The ASIC is a low-power signal processor –its core consumes only $(0.37\mu\text{W/tap})f_s$, where f_s is the servo rate in kHz. The efficient hardware implementation that produces these low power requirements is described in [5]. We focus on designing the filters in Fig. 19 and subsequently demonstrate the closed-loop performance with this ASIC and a microgyro.

The AGC is nonlinear, however, the distinct time scales in the closed-loop system –a fast oscillator frequency and a slower time scale for the modulated amplitude– can be exploited to analyze the closed-loop system response as demonstrated in [14], [6]. These references analyze the continuous-time case shown in Fig. 18 and reveals how the response of the oscillator depends upon the various controller parameters. In contrast to the thoroughly analyzed continuous-time models, the ASIC filters are purely discrete-time and FIR. The discrete-time implementation is pursued because of the flexibility it imparts to the ASIC for adapting to a wide range of sensor dynamics. The choice of FIR filters is due to the desire to avoid limit cycling because all computations use fixed-point arithmetic. Consequently, rigorous analysis of the closed-loop system consisting of a sampled-data sensor model and a controller employing fixed-point implementations of FIR filters is quite complicated and one relies on simulation to identify issues associated with over/underflow and scaling.

The main features of the architecture in Fig. 19 are 1) the seven, 128-tap, fully programmable FIR filters and a proportional-integral section for the automatic gain control, 2) fixed-point computation with 18-bit input data precision, 18-bit output data precision, 18-bit coefficient precision, and 20-bit internal data precision (24-bits for the integrator), and 3) programmable gains K_1 through K_8 that can implement the T_{in} and T_{out} transformations discussed in Section III-A. The AGC consists of FIR1, the rectifier, FIR2, the proportional-integral (PI) compensation and programmable limiters on the integrator and AGC gain. The rebalance loop compensation is implemented by FIR3. The ASIC is hosted on a brassboard that also contains the signal converters and an interface to program the ASIC from a personal computer. A high performance, 24-bit, audio codec provides the analog-to-digital and digital-to-analog conversion. The brassboard also hosts the antialiasing and smoothing filters, and six 12-bit ADCs for gyro biasing.

The decoupled sensor dynamics in a neighborhood of 4420 Hz permits a greatly simplified design process because the off-diagonal terms in Fig. 17 can be ignored. The wide-band response in Fig. 9 demonstrates that large loop gain can be achieved in a neighborhood of 2705Hz and 4420Hz with relatively modest controller gain. In the sequel, the sensor is designated by P, the control hardware with ASIC filters is designated by C, and the ijth channel of P is denoted P_{ij}, with the same convention applying to C. Our design process ignores the off-diagonal coupling in both C and P but the analysis of the designs in Fig. 23 includes the coupling effects at least from the point of view of nominal stability. The automatic gain controller is defined by specifying FIR1, FIR2, the reference amplitude R, and the gains K_P and K_I. The plant model for this loop is the $(1,1)$ channel in Fig. 17.

A useful heuristic emerged from [14] that is somewhat independent of the filter implementation details and that may be applied here to the design of the AGC filters: the two-time scale behavior of the closed-loop system allows us to design the AGC filters by assuming the compensator is a fixed, linear filter. That is, from the sensor's perspective, the compensation can be treated as a fixed filter for any given sensor response because the resonances in the sensor are much higher in frequency than the bandwidth of the AGC gain. Here we refer to the *AGC gain* as the subsystem that modulates the feedback signal in Fig. 19 to distinguish it from the *compensator* that is defined as the AGC gain times FIR1. A typical AGC gain as a function of its input signal amplitude is shown in Fig. 20. This gain modulates the output of FIR1 to determine the control effort. Using this as a guide, we design FIR1 to adjust the loop gain phase to be zero at the higher frequency rocking mode so under positive feedback this mode is destabilized, but as the amplitude approaches the reference value, the AGC gain is reduced as seen in Figure 20. Furthermore, the compensation is also designed to attenuate the translational mode near 2.7 kHz. The loop gain for the AGC channel ($P_{11}C_{11}$ using our notation) is shown in Figure 21.

The rebalance loop is a linear, high-gain filter implemented by FIR3. One objective of this loop is to achieve disturbance rejection at the 2.7 kHz translational mode. The primary
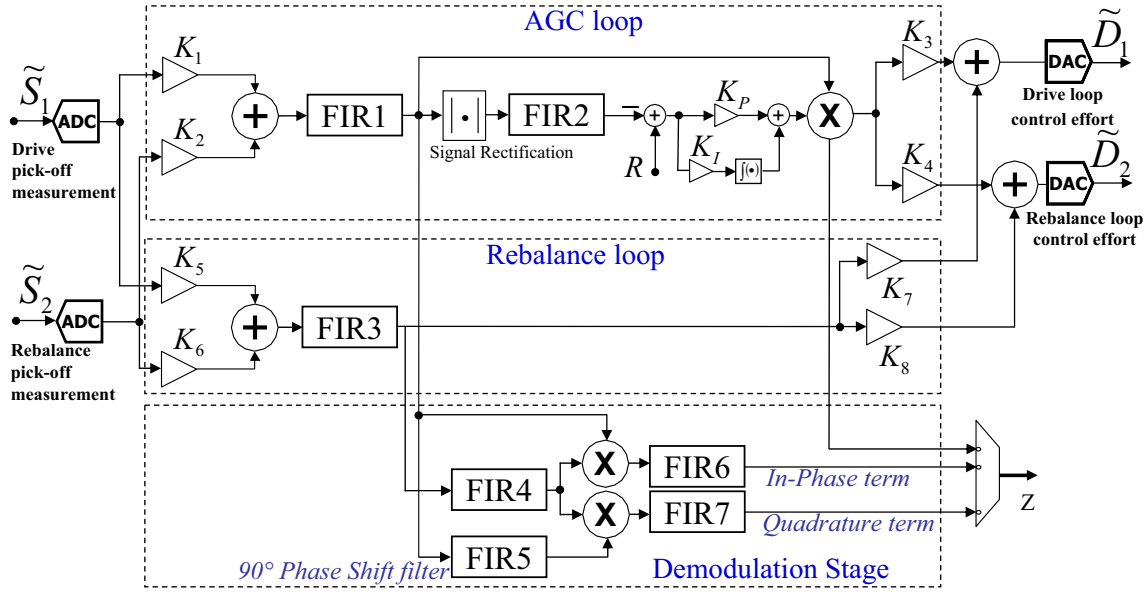
Fig. 19. The ASIC employs eight programmable 128-tap FIR filters in addition to the PI compensation for the AGC.
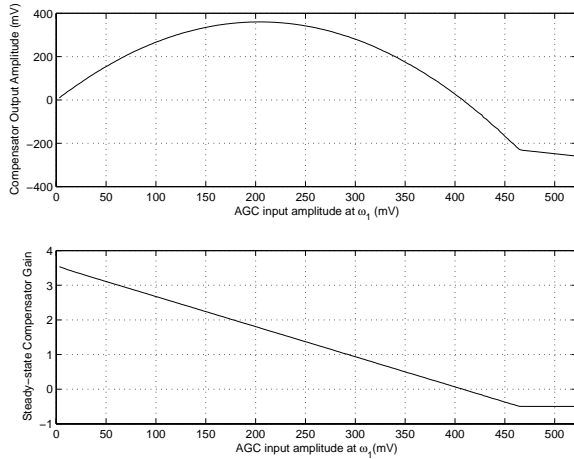

Fig. 20. The steady state properties of the AGC are shown in two formats. The top plot shows the compensator output amplitude as a function of the input amplitude when the input is a sinusoid corresponding to the higher frequency rocking mode (approximately 4428 Hz). Very little excitation amplitude is required to maintain a constant amplitude response for this mode so the sensor's final amplitude is very near where the graph crosses zero. The bottom plot is the *AGC gain* and is the top plot normalized by the input magnitude.
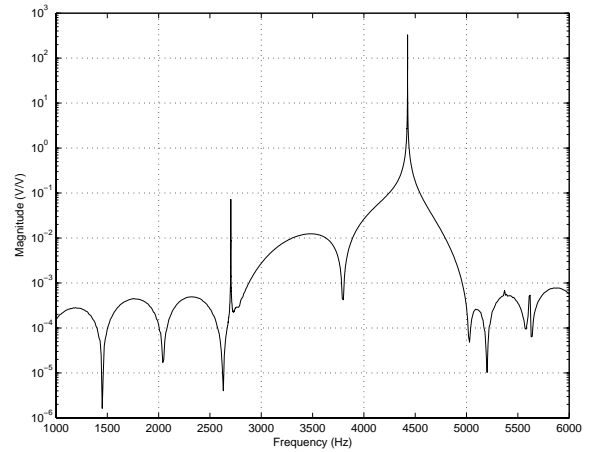

Fig. 21. $P_{11}C_{11}$ using empirical sensor and control hardware data. The AGC excites the higher frequency rocking mode by proper shaping of the loop phase (not shown). The second rocking mode is not excited because of the decoupling achieved in the plant, cf. Figure 17, and the translational mode at 2.7 kHz is attenuated and not regulated by the AGC.

control, however, is to reject the Coriolis-induced disturbance at the 4423 Hz rocking mode caused by sensor rotation. As in the AGC design, there are interpolation constraints on the phase of the control filters at these modes in order to achieve optimal damping of the modes. Figure 22 shows the loop gain $P_{22}C_{22}$ associated with the rebalance channel.

The ASIC filters were designed without regard to cross-coupling in the controller. Subsequent tests of the ASIC have confirmed that peak magnitudes of the off-diagonal terms are approximately -80dB. In other words, $\max_\omega |C_{pq}| \approx -80$dB, $p \neq q$ – these results are not shown for sake of brevity. The small off-diagonal magnitudes justifies neglecting these terms in the design process. The off-diagonal terms in the plant, however, can be more problematic. These terms are the $(1,2)$ and $(2,1)$ channels in Figure 17. Furthermore, the translation mode near 2.7 kHz couples strongly into all channels in the sensor. Thus, a more rigorous argument for
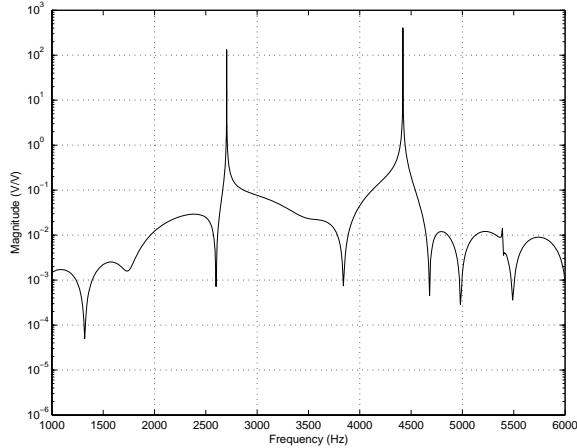
Fig. 22. The magnitude of the rebalance channel, P_2C_{22}, is shown. This channel regulates both the lower frequency rocking mode (~ 4423 Hz) and the translational mode (~ 2.7 kHz) to zero using linear high gain feedback.

Fig. 23. Yes, this really is a Nichols chart. It represents the loci of $\det(I - P\Delta C)$ for $\Delta = [\delta, 0; 0, 1]$, $\delta = \{1, 1/10, 1/328\}$, where δ represents a scale of the maximum AGC gain (the rebalance gain is fixed), P is the decoupled sensor dynamics (Figure 17), and C is the controller. The frequency span covers 1 kHz to 6 kHz and the empirical frequency response data of the sensor and controller are used to create these plots. The plots corresponding to the AGC gains $\{1, 1/10\}$ imply that the closed-loop system has two unstable closed-loop poles. When the AGC gain is reduced to $1/328$ the return difference determinant passes through the origin indicating a sustained oscillation is achieved. The frequency markers reveal that the higher frequency rocking mode is excited as intended ($\omega_{A1} = 4427.63$ Hz and $\omega_{A2} = 4427.64$ Hz.)

Fig. 24. AGC transients when loops are closed about a quiescent sensor.

the stability condition of the closed-loop system for different AGC gains is desired and can be obtained by application of the multivariable Nyquist criterion using all channels of plant (sensor) and controller (ASIC plus brassboard hardware) frequency response data. This criterion does not explore the robustness of the stability condition (namely, destabilize the higher frequency rocking mode, but dampen the other rocking mode and translational mode) but answers more definitively the nominal stability condition. A Nichols chart of the return difference for various values of the AGC gain is the easiest way to view the results. This chart is shown in Fig. 23 and reveals that the AGC does indeed initially destabilize the mode at 4428 Hz when the loop is closed about a quiescent sensor (AGC measurement signal is much smaller than the reference value upon loop closure and corresponds to $\delta = 1$ in the figure). As the amplitude of this mode grows, the AGC gain is reduced (see $\delta = 0.1$) until the desired reference value for the response amplitude is achieved, at which point the AGC causes the return difference to pass through the origin at a frequency very near 4428 Hz.

When both AGC and rebalance loops are closed about a quiescent sensor, the transients in Fig. 24 are recorded. Ideally, the $\tilde{S}_2$ and $\tilde{D}_2$ signals are completely decoupled from the AGC signals ($\tilde{S}_1$ and $\tilde{D}_1$). This is largely the case, although some cross coupling does occur in the sensor. The $\tilde{S}_1$ signal is essentially the isolated rocking mode at 4428 Hz responding to the AGC feedback. Its initial growth rate is easily predicted from simple sensor frequency response and AGC parameters. Steady state is reached after 0.05 seconds where it is noted that the drive amplitude is quite small due to the very light damping. The bandwidth of the AGC is 26 Hz and is tested by applying a small perturbation to the reference value. The advantage of the AGC is revealed in Fig. 25 where it is shown how the controller tracks the shifts
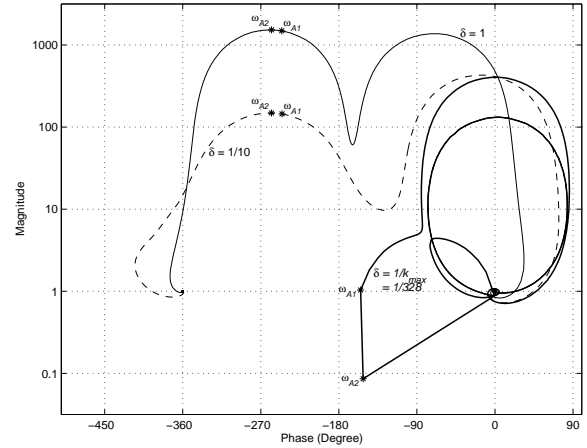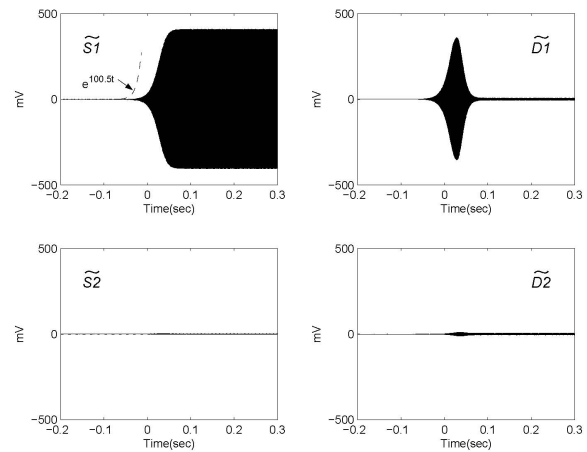
in modal frequency over a period of 1 hour. Snapshots of the dynamics at different times were shown in Figure 16 yet the AGC is able to follow the trend. This is indeed confirmed by the fact that the AGC control effort magnitude changes by only 5% over the same interval.

The performance of the rebalance loop is quantified by measuring the closed-loop sensitivity function for the (2,2) channel. Due to the decoupled plant dynamics in a neighborhood of ω_1 and ω_2, and because of the low gain of the AGC loop at ω_3, we can treat this channel is linear even when the
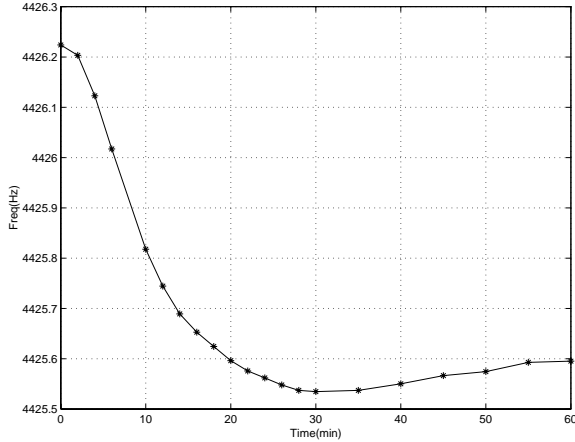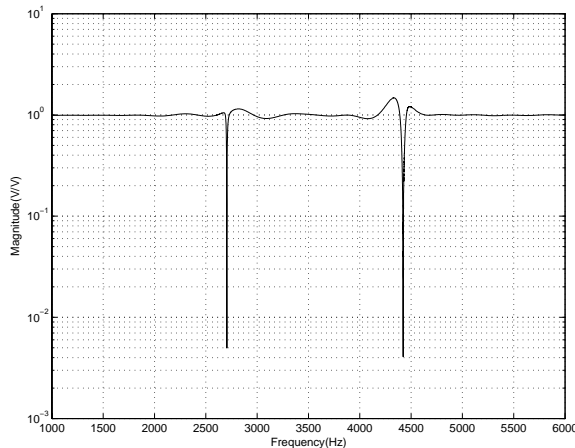
Fig. 25.   Frequency tracking of the AGC loop.

Fig. 26.   Sensitivity of $(2,2)$ channel.

AGC is operational. Furthermore the $(2,2)$ channels of the input and output sensitivity functions are equal (the controller is diagonal) so only one measurement is made and shown in Fig. 26. Since the loop gain $P_{22}C_{22}$ can be made greater than one only in a neighborhood of the rocking mode and translational mode, the reduction in sensitivity occurs near these frequencies. The primary objective of the rebalance control is to regulate rocking mode at 4423 Hz to zero and the sensitivity function can be used to quantify the closed-loop time constant. In fact, the 50 dB of attenuation at 4423 Hz corresponds to a closed-loop bandwidth of 20 Hz. It is also evident from the sensitivity plot that disturbance rejection of -45 dB is achieved at 2.7 kHz.

IV. REFERENCES

[1] Bae, S.Y., Hayworth, K.J., Yee, K.Y., Shcheglov, K., and Wiberg, D.V., "High performance MEMS microgyroscope," *Proc. of SPIE*, Vol. 4755, pp. 316–24, 2002.

[2] Chen, Y.-C., Hui, J., and M'Closkey, R.T., "Closed-loop Identification of a Micro-sensor," Accepted *IEEE Conference on Decision and Control,* Dec. 2003, Maui, HI.

[3] Chen, Y.-C., M'Closkey, R.T., Tran, T., and Blaes, B.,"A control and signal processing integrated circuit for the JPL-Boeing micromachined gyroscopes," *Submitted*. Contact first author for draft.

[4] Fell, C., Hopkin, I., Townsend, K., "A Second Generation Silicon Ring Gyroscope," *Proc. Symposium Gyro Technology*, 1999, Stuttgart, Germany.

[5] Grayver, E. and Daneshrad, B., "Word-serial Architectures for Filtering and Variable Rate Decimation," *VLSI Design*, Vol. 14(4). pp. 363–72, 2002.

[6] Grayver, E., and M'Closkey, R.T., "Automatic Gain Control ASIC for MEMS Gyro Applications," *Proc. 2001 American Control Conference*, Vol. 2, pp. 1219–22, 2001.

[7] Janson, S., Helvajian, H., Amimoto, S., Smit, G., Mayer, D., Feuerstein, S., "Microtechnology for space systems," *1998 IEEE Aerospace Conf. Proc.*, Vol. 1, pp. 409-18, 1998.

[8] Kourpenis, A., Connelly, J., and Sitomer, J., "Low Cost MEMS Inertial Measurement Unit," in Proc. National Technical Meeting 2004, Institute Of Navigation, 26-28 January 2004, San Diego, CA.

[9] Kubena R.L., Atkinson G.M., Robinson W.P., Stratton F.P., "A new miniaturized surface micromachined tunneling accelerometer," *IEEE Electron Device Letters*, Vol. 17, No. 6, pp. 306–8, 1996.

[10] Kubena R.L., Vickers-Kirby D.J., Joyce R.J., Stratton F.P., "A new tunneling-based sensor for inertial rotation rate measurements," *J. Microelectromechanical Systems*, Vol.8, No.4, pp. 439–47, 1999.

[11] Lawrence, A., *Modern Inertial Technology: Navigation, Guidance, and Control.* Springer-Verlag, New York, 1998.

[12] Leland, R.P., "Adaptive mode tuning for vibrational gyroscopes," *IEEE Trans. Control Systems Tech.*, vol.11, no.2, pp.242–7, March 2003.

[13] Lynch, D. D., "Vibratory Gyro Analysis by the Method of Averaging," *The 2nd Saint Petersburg Intl. Conf. on Gyroscope Technology and Navigation,* pp. 26-34, May 24–5, 1995.

[14] M'Closkey, R.T., Vakakis, A., and Gutierrez, R., "Mode Localization Induced by a Nonlinear Control Loop," *Nonlinear Dynamics,* Vol. 25, No. 1, pp. 221–36, 2001.

[15] M'Closkey, R.T., Gibson, J.S., and Hui, J., "System identification of a MEMS gyroscope," *Journal of Dy-

namic Systems, Measurement, and Control, Transactions of the ASME, Vol.123, No.2, pp. 201–10, 2001.

[16] Madni, A.M., Costlow, L.E., and Knowles, S.J., "Common Design Techniques for BEI GyroChip Quartz Rate Sensors for Both Automotive and Aerospace/Defense Markets," *IEEE Sensors Journal*, Vol. 3, No. 5, pp. 569–78, 2003.

[17] McFarlane, D.C, and Glover, K., *Robust controller design using normalized coprime factor plant descriptions*, Springer-Verlag, New York, 1990.

[18] Morrow, C.T., "Zero Signals in the Sperry Tuning Fork Gyrotron," *The Journal of Acoustic Society of America,* Vol. 27, No. 3, pp. 581–5, 1955.

[19] Newton, G.C. Jr., "Theory and Pratice in Vibratory Rate Sensor," *Control Engineering,* pp. 95–9, 1963.

[20] Painter C.C., Shkel A.M., "Active structural error suppression in MEMS vibratory rate integrating gyroscopes," *IEEE Sensors Journal*, vol.3, no.5, pp.595–606, 2003.

[21] Tang, T.K., Gutierrez, R.C., Wilcox, J.Z., Stell, C., Vorperian, V., Dickerson, M., Goldstein, B., Savino, J.L., Li, W.J., Calvet, R., Charkaborty, I., Bartman, R., and Kaiser, W.J., "Silicon Bulk Micromachined Vibratory Gyroscope for Microspacecraft," *SPIE-Int. Soc. Opt. Eng. Proceedings of SPIE - the International Society for Optical Engineering,* vol. 2810, pp.101–15, 1996.

[22] Tang, T.K., Gutierrez, R.C., Wilcox, J.Z., Stell, C., Vorperian, V., Calvet, R., Li, W.J., Charkaborty, I., Bartman, R., and Kaiser, W.J., "Silicon Bulk Micromachined Vibratory Gyroscope," *Solid-State Sensor and Actuator Workshop, Hilton Head, SC*, pp. 288–93, 1996.

[23] Tang, T.K., Gutierrez, R.C., Stell, C.B., Vorperian, V., Arakaki, G.A., Rice, J.T., Li, W.J., Chakraborty, I., Shcheglov, K., Wilcox, J.Z., and Kaiser, W.J., "A Packaged Silicon MEMS Vibratory Gyroscope for Microspacecraft," *Proc. IEEE, The Tenth Ann. Intern. Workshop Micro Electro Mech. Sys.*, pp. 500–5, 1997.